Concentration dependence of Li^+/Na^+ diffusion in manganese hexacyanoferrates

Masamitsu Takachi[1], Yuya Fukuzumi[1], and Yutaka Moritomo[1,2]*

[1]*Graduate School of Pure and Applied Science, University of Tsukuba, Tsukuba, Ibaraki 305-8571, Japan*
[2]*Center for Integrated Research in Fundamental Science and Engineering (CiRfSE), University of Tsukuba, Tsukuba, Ibaraki 305-8571, Japan*

Manganese hexacyanoferrates (Mn-HCFs) with the jungle-gym-type structure are promising cathode materials for Li^+/Na^+ secondary batteries (LIBs/SIBs). Here, we investigated the diffusion constants D^{Li}/D^{Na} of Li^+/Na^+ against the Li^+/Na^+ concentration x^{Na}/x^{Li} and temperature (T) of $A_{1.32}Mn[Fe(CN)_6]_{0.83}3.6H_2O$ (A = Li and Na). We evaluated the activation energy E_a^{Li}/E_a^{Na} of D^{Li}/D^{Na} against x^{Na}/x^{Li}. We found that E_a^{Na} steeply increases with x^{Na} from 0.41 eV at $x^{Na} = 0.69$ to 0.7 eV at 1.1. The increase in E_a^{Na} is ascribed to the occupancy effect of the Na^+ site. The increase in E_a^{Li} is suppressed, probably because the number of Li^+ sites is three times that of Na^+ site.

1. Introduction

Coordination polymers are promising cathode materials for lithium-ion/sodium-ion secondary batteries (LIBs/SIBs),[1,2] owning to their robust nature of their three-dimensional (3D) frameworks against Li^+/Na^+ intercalation/deintercalation. Among the coordination polymers, transition metal hexacyanoferrates (M–HCFs: $A_xM[Fe(CN)_6]_y$, A and M are alkali and transition metals, respectively) are most intensively investigated[3–11] as cathode materials for LIBs[12–19] and SIBs.[20–29]

A thin-film electrode of Mn-HCF, $Li_xMn[Fe(CN)_6]_{0.83}3.5H_2O$, exhibits high capacity (Q = 128 mAh/g) with excellent cyclability.[14] The material exhibits redox reactions of Fe and Mn without structural phase transition in the entire x-region ($0.00 \leq x \leq 1.32$).[30] The capacity further increases with increasing $[Fe(CN)_6]$ concentration (y) from 115 mAh/g at $y = 0.81$ to 143 mAh/g at 0.93.[31] In addition, the Li^+ diffusion constant ($D^{Li} = 2 \times 10^{-10}$ cm^2 s^{-1})[32] of $Li_xMn[Fe(CN)_6]_{0.81}\cdot 3.0H_2O$ is much larger than those of conventional cathode materials: $D^{Li} = 10^{-12}$ - 10^{-11}cm^2 s^{-1} for $LiCoO_2$[33] with a layered rock-salt structure, 10^{-13} - 10^{-12}cm^2 s^{-1} for $LiFePO_4$[34] with an olivine structure, and 10^{-12} - 10^{-10}cm^2 s^{-1} for $LiMn_2O_4$[35] with a spinel structure. Actually, Moritomo *et al.*[36]

*E-mail: moritomo@sakura.cc.tsukuba.ac.jp

reported that the discharge rate of a thin-film electrode of $Li_xMn[Fe(CN)_6]_{0.81}3.0H_2O$ reaches 3000 C. On the other hand, Lu *et al.*[20] reported Na^+ intercalation behaviors in a K-M-$Fe(CN)_6$ system (M = Mn, Fe, Co, No, Cu, Zn), even though the Coulomb efficiency of the system is very low. The Coulomb efficiency is significantly improved in thin films of $Na_{1.32}Mn[Fe(CN)_6]_{0.83}3.5H_2O$,[21] and $Na_{1.6}Co[Fe(CN)_6]_{0.9}2.9H_2O$:[22] the films show high capacities of 109 and 135 mAh/g and average operating voltages of 3.4 and 3.6 V against Na, respectively.

Most of the M-HCFs show to the face-centered cubic structure with the three-dimensional (3D) jungle-gym-type framework,[37,38] casing periodic cubic nanopores, ≈ 0.5 nm at the edge. For convenience of explanation, we will call a cubic nanopore a *nanocube*. The framework consists of transition metals (M and Fe) and cyano groups (CN) that covalently bridges the neighboring transition metals as - M - NC - Fe - . Significantly, the framework can accommodate guest ions, such as Li^+, Na^+, K^+, Rb^+, Cs^+, Ca^{2+}, Mg^{2+}, and Sr^{2+}.[39–46] The framework can be used to decontaminate the living environment of radioisotopes such as $^{137}_{55}Cs^+$.[41,42] Larger guest ions, *e.g.*, K^+, Rb^+, and Cs^+, are located at the center of the nanocube[37,38] while smaller Na^+ is located at the tetrahedral site close to the central position of the nanocube.[47,48] In these crystal structures, each nanocube can accommodate one guest ion. That is, the guest ion sites are fully occupied when the guest concentration x reaches 2. Interestingly, Li^+ seems to be too small to locate around the central position of the nanocube. Actually, the central region of the nanocube of $Li_{0.9}Mn[Fe(CN)_6]_{0.83}3.5H_2O$[21] is occupied by crystal waters, suggesting that Li^+ is located at the face of the nanocube. Then, the number of Li^+ sites is three times that of Na^+ sites.

The significant features of M-HCF are the folloings, (1) The jungle-gym-type framework is structurally stable even at $x = 0$ and (2) Na^+ is electrochemically replaced by Li^+ without a change in the chemical composition of the framework. Therefore, a thin film electrode of M-HCF gives us an ideal platform for directly comparing the diffusion dynamics of Li^+ ($r = 0.92$ Å) and Na^+ ($r = 1.18$ Å) within the same host framework. Unfortunately, Co-HCF ($Li_xCo[Fe(CN)_6]_{0.9}2.9H_2O$[15]) shows a first-order structural phase transition of the framework with decreasing x and is not suitable for the present investigation. In our previous paper,[49] we investigated the framework size dependence of Na^+ diffusion constant D^{Na} and its activation energy E_a^{Na} in M-HCFs. We found that D^{Na} (E_a^{Na}) systematically increases (decreases) with increasing the framework size.

In this paper, we systematically investigated D^{Li}/D^{Na} against Li^+/Na^+ concentra-

tion $x^{\mathrm{Na}}/x^{\mathrm{Li}}$ and temperature T in the same Mn-HCF framework. By *ex situ* X-ray absorption spectroscopy (XAS) around the K-edge, we determined the valence state of Fe and Mn against $x^{\mathrm{Na}}/x^{\mathrm{Li}}$. We evaluated the activation energy $E_{\mathrm{a}}^{\mathrm{Li}}/E_{\mathrm{a}}^{\mathrm{Na}}$ of $D^{\mathrm{Li}}/D^{\mathrm{Na}}$ against $x^{\mathrm{Na}}/x^{\mathrm{Li}}$. We ascribed the steep increase in $E_{\mathrm{a}}^{\mathrm{Na}}$ with x^{Na} to the occupancy effect of the Na^+ site. The increase in $E_{\mathrm{a}}^{\mathrm{Li}}$ is suppressed, probably because the number of Li^+ sites is three times that of Na^+ sites.

2. Experimental methods

2.1 Film preparation

Mn-HCF films were fabricated by their electrochemical deposition on indium tin oxide (ITO) transparent electrodes under potentiostatic conditions at - 0.45 V vs. a standard Ag/AgCl electrode.[15,19] The electrolytes were aqueous solutions containing 1.0 mM $K_3[Fe^{III}(CN)_6]$, 1.5 mM $Mn^{II}Cl_2$, and 1 M NaCl. The obtained film was transparent with a thickness (d) of $\approx$ 500 nm. The chemical composition of the Mn-HCF film was determined to be $Na_{1.36}Mn^{II}[Fe^{II}(CN)_6]_{0.84}3.4H_2O$ (denoted as NMF84). Calcd: Na, 9.7; Mn, 16.9; Fe, 14.5; C, 18.7; H, 2.1; N, 21.8%. Found: Na, 10.6; Mn, 16.8; Fe, 14.7; C, 18.2; H, 2.1; N, 20.9%. The Li analogue (LMF84: $Li_{1.36}Mn^{II}[Fe^{II}(CN)_6]_{0.84}3.4H_2O$) of NMF84 was electrochemically prepared by Na^+ deintercalation and Li^+ intercalation.

The X-ray powder diffraction (XRD) patterns of the as-grown NMF84 film was obtained using of a synchrotron-radiation X-ray source. The crystal structure was trigonal ($R\underline{3}$m; $Z = 3$) with $a_{\mathrm{H}}\sqrt{2}$ = 10.603(1) Å and $c_{\mathrm{H}}/\sqrt{3}$=10.429(2) Å. The morphology of the as-grown film was investigated on the basis of scanning electron microscopy (SEM) images (TECHNEX Mighty-8). Each grain, whose in-plane size is $\approx$ 0.5 μm, extends from the collecting ITO electrode to the film surface. Therefore, the grain boundary effect is negligible in the analysis of complex impedance spectra (CIS).

2.2 Control of $x^{\mathrm{Na}}/x^{\mathrm{Li}}$

x^{Na} was controlled by the charge or discharge processes in a handmade beaker-type two-pole cell. The NFM84 film and the Na metal were used as the cathode and anode, respectively. The active areas of the films were about 1.0 cm^2. The electrolyte was carbonate/diethyl carbonate (EC/DEC) containing 1 M $NaClO_4$. We confirmed that the discharge capacity (= 111 mAh/g) of the NMF84 film was close to the ideal value (= 112 mAh/g) for the Na^+ intercalation from x = 0.0 to 1.36. The magni-

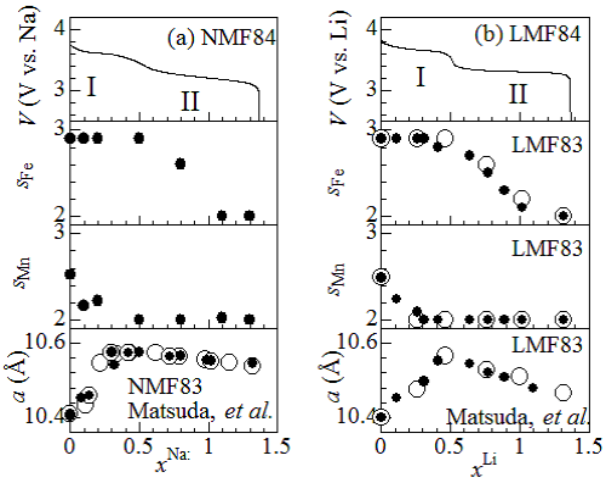

Fig. 1. (a) Discharge curve, average Fe valence (s_{Fe}), and average Mn valence (s_{Mn}) in the $Na_xMn[Fe(CN)_6]_{0.84}3.4H_2O$ (NMF84) films against Na^+ concentration (x^{Na}). The error bars are within the symbol size. For convenience of explanation, we defined plateaus I and II. In the bottom panel, the lattice constant (a) of $Na_xMn[Fe(CN)_6]_{0.83}3.5H_2O$ (NMF83) are replotted from Ref.[21] The open and filled marks mean that the data were obtained in the charge and discharge runs, respectively. (b) Discharge curve of the $Li_xMn[Fe(CN)_6]_{0.84}3.4H_2O$ (LMF84) film against Li^+ concentration (x^{Li}). For convenience of explanation, we defined plateaus I and II. In the middle panel, s_{Fe} and s_{Mn} of the $Li_xMn[Fe(CN)_6]_{0.83}3.5H_2O$ (LMF83) films are evaluated from the XAS reported in Ref.[30] The error bars are within the symbol size. In the bottom panel, a of LMF83 are replotted from Ref.[30] Open and filled marks mean that the data were obtained in the charge and discharge runs, respectively.

tudes of x^{Na} was evaluated from the relative charge assuming the ideal redox reaction. The top panel of Fig. 1(a) shows the discharge curve of the NFM84 film. The cut-off voltage was in the range from 2.0 to 4.2 V. The plateaus I and II are ascribed to $1.36Na^+ + Mn^{II}_{0.48}Mn^{III}_{0.52}[Fe^{III}(CN)_6]_{0.84} \rightarrow 0.84Na^+ \; Na_{0.52}Mn^{II}[Fe^{III}(CN)_6]_{0.84}$ and $0.84Na^+ \; Na_{0.52}Mn^{II}[Fe^{III}(CN)_6]_{0.84} \rightarrow Na_{1.36}Mn^{II}[Fe^{II}(CN)_6]_{0.84}$, respectively.[21]

x^{Li} was controlled by the charge or discharge processes in a handmade beaker-type two-pole cell. The LFM84 film and the Li metal were used as the cathode and anode, respectively. The active areas of the films were about 1.0 cm^2. The electrolyte was EC/DEC containing 1 M $LiClO_4$. We confirmed that the discharge capacity (= 107 mAh/g) of the LMF84 film was close to the ideal value (= 119 mAh/g) for the Li^+ intercalation from x = 0.0 to 1.36. The magnitudes of x^{Li} was evaluated from the relative charge assuming the ideal redox reaction. The top panel of Fig. 1(b) is the discharge curve of the LFM84 film. The cut-off voltage was in the range from 2.0 to 4.2 V. The plateaus I and II are as-

cribed to $1.36Li^+ + Mn^{II}_{0.48}Mn^{III}_{0.52}[Fe^{III}(CN)_6]_{0.84} \rightarrow 0.84Li^+ Na_{0.52}Mn^{II}[Fe^{III}(CN)_6]_{0.84}$ and $0.84Li^+ Na_{0.52}Mn^{II}[Fe^{III}(CN)_6]_{0.84} \rightarrow Li_{1.36}Mn^{II}[Fe^{II}(CN)_6]_{0.84}$, respectively.[14,30] In plateau I, the complex impedance spectra (CIS) are too deformed to analyze.

2.3 Complex impedance spectroscopy

To investigated the Li^+/Na^+ diffusion kinetics, CIS were measured with a potentiostat (BioLogic SP-150) in a two-pole beaker-type cell against Li/Na metal. The electrolyte is EC/DEC containing 1M $LiClO_4$ for Li^+ and EC/DEC containing 1M $NaClO_4$ for Na^+. The active area of the film was 1 cm^2. The frequency range was from 5 mHz to 200 kHz, and the amplitude was 30 mV. The T-dependence of CIS was measured in the heating run at a fixed x^{Li}/x^{Na}. We confirmed that the temperature variation of CIS was recovered when the film was cooled to its initial temperature. We measured the T-dependence of CIS against x^{Na} using the same NMF84 film (d = 400 nm). We measured the T-dependence of CIS against x^{Li} using the same LMF84 film (d = 400 nm).

2.4 *Ex situ* X-ray absorption spectroscopy

The electronic states of Fe and Mn were investigated by *ex situ* XAS measurement around the K-edges. The XAS measurements were conducted at beamline 12C of the Photon Factory, KEK. The wavelengths of the monochromator were calibrated with the absorption edge of Fe/Mn foil. The NMF84 films with controlled x^{Na} were sealed in plastic in a glove box to avoid air exposure. The XAS spectra of the films were recorded using a Lytle detector in a fluorescent yield mode with a Si(111) double-crystal monochromator at 300 K. The background subtraction, normalization, and component decomposition were performed using the ATHENA program.[50]

3. Results

3.1 Average valence of Fe and Mn against x^{Li}/x^{Na}

Figure 2(a) shows the XAS spectra of the NMF84 films around the Fe K edge against x^{Na}. The electronic configuration of the as-grown film (x^{Na} = 1.3) is Fe^{2+} - Co^{2+}. The Fe K-edge spectra at x^{Na} = 0.0 and 1.3 coincide with those of Fe^{2+} (S = 1/2) and Fe^{2+} (S = 0).[51] Under the charge neutrality condition, the electronic configuration at x^{Na} = 0.0 is Fe^{3+} - $Mn^{2.52+}$: $Na_{1.36}Mn^{2+}[Fe^{2+}(CN)_6]_{0.84}3.4H_2O \rightarrow 1.36Na^+ +$

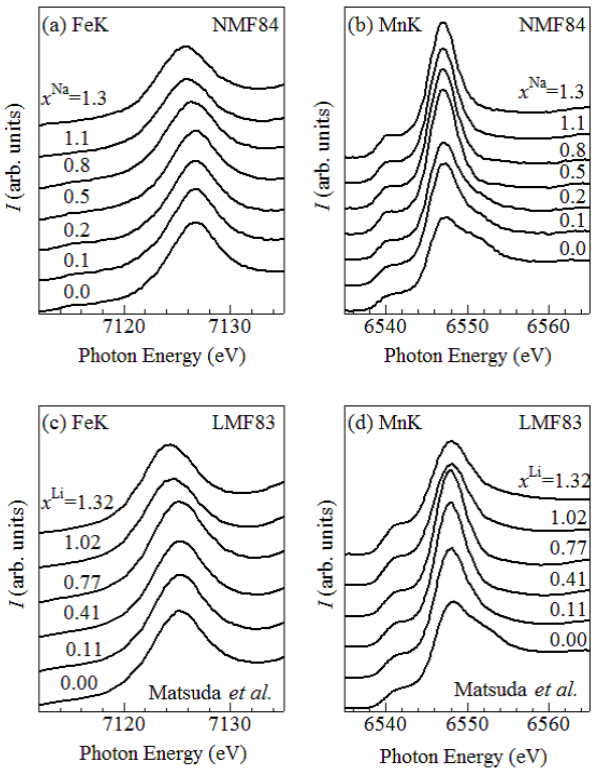

Fig. 2. XAS spectra around the (a) Fe K- and (b) Mn K-edges in the NMF84 films against x^{Na}. XAS spectra around the (a) Fe K- and (b) Mn K-edges in the $\mathrm{Li}_x\mathrm{Mn}[\mathrm{Fe}(\mathrm{CN})_6]_{0.83}3.5\mathrm{H_2O}$ (LNF83) films against x^{Li}. The spectra in (c) and (d) are replotted from Ref.[30)]

$\mathrm{Mn}^{2+}_{0.48}\mathrm{Mn}^{3+}_{0.52}[\mathrm{Fe}^{3+}(\mathrm{CN})_6]_{0.84}3.4\mathrm{H_2O}$. The XAS spectra show a slight blue-shift with increasing x^{Na}, indicating the partial formation of Fe^{2+}. The average Fe valence (s_{Fe}) was determined from the peak energy E:

$$s_{\mathrm{Fe}} = \Delta E + 2, \tag{1}$$

where ΔE (eV) is the energy shift from the fully discharged state ($x^{\mathrm{Na}} = 1.3$). We further evaluated s_{Fe} in the $\mathrm{Li}_x\mathrm{Mn}[\mathrm{Fe}(\mathrm{CN})_6]_{0.83}3.5\mathrm{H_2O}$ (LNF83) films against x^{Li} using the Fe K-edge spectra in the literature.[30)] The thus-obtained s_{Fe} is plotted in the middle panels of Figs. 1(a) and 1(b).

Figure 2(b) shows the XAS spectra of the NMF84 films around the Mn K-edge against x^{Na}. The XAS shows significant change in $0.0 \leq x^{\mathrm{Na}} \leq 0.5$, indicating variation of the Mn valence s_{Mn}. Assuming that $s_{\mathrm{Mn}} = 2$ at $x^{\mathrm{Na}} = 1.3$ and 2.5 at 0.0, we evaluated s_{Mn} from the spectral decomposition as:

$$\phi(x^{\mathrm{Na}}) = (2s^{\mathrm{Mn}} - 4)\phi(0.0) + (5 - 2s^{\mathrm{Mn}})\phi(1.3), \tag{2}$$

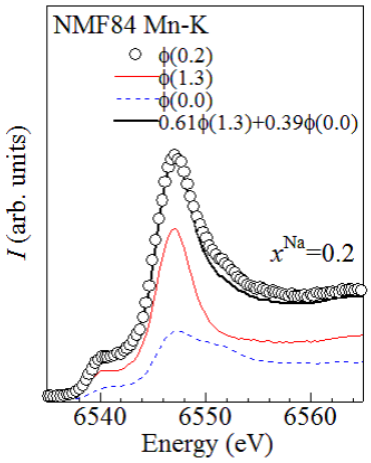

Fig. 3. (Color online) Spectral decomposition of the Mn K edge spectrum of the NMF84 film. The XAS spectrum [$\phi(x^{\mathrm{Na}})$] at $x^{\mathrm{Na}} = 0.2$ are decomposed to $\phi(0.0)$ and $\phi(1.3)$. Thin solid and broken curves are $\phi(1.3)$ and $\phi(0.0)$, respectively. Open circles and thick solid curves represent $\phi(0.2)$ and the linear combination of $\phi(0.0)$ and $\phi(1.3)$, respectively.

where $\phi(x^{\mathrm{Na}})$ is the Mn K-edge spectrum at x^{Na}. Figure 3 shows an example of spectral decomposition. We further evaluated s_{Mn} in the LMF83 films against x^{Li} using the Mn K-edge spectra in the literature.[30] The thus-obtained s_{Mn} is plotted in the middle panels of Figs. 1(a) and 1(b).

In plateau I of NMF84 [Fig. 1(a)], the Mn valence steeply decreases from +2.5 to +2 with increasing x^{Na} while the Fe valence remains +3. In plateau II of NMF84 [Fig. 1(a)], the Fe valence steeply decreases from +3 to +2 with increasing x^{Li} while the Mn valence remains +2. Therefore, the plateaus I and II can be ascribed to the reduction of Mn and Fe, respectively. These assignments of the plateaus in the NMF84 film is the same as those in the LMF84 film [Fig. 1(b)].

3.2 Randles equivalence circuit analysis of CIS

Figure 4(a) shows prototypical examples of CIS of the NMF84 film at x^{Na} =0.7. In the high-frequency region, the CIS show a semicircle. With the decrease in the frequency f, the CIS form straight lines with the angle of $\pi/4$ against the real axis [broken straight line]. With further decreases in f, the CIS deviate from the broken line. A similar behavior is observed in the LMF84 film at x^{Li} =0.7 [Fig. 4(b)] even though the semicircles in the high-frequency region are fairly squashed. Let us define the critical frequency f_{c} at which CIS start to deviate from the broken line. Then, f_{c}^{-1} is the characteristic time when the diffusion length of Na^{+} reaches the film thickness d. The

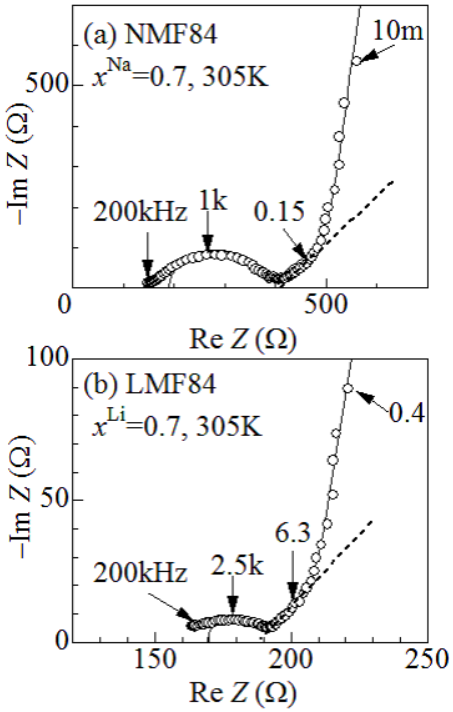

Fig. 4. Complex impedance spectra of (a) NMF84 ($x^{\mathrm{Na}} = 0.7$) and (b) LMF84 ($x^{\mathrm{Li}} = 0.7$) at 305 K. Arrows indicate the frequencies. Broken straight lines are guided to the eye. Solid curves are results of the least-squares fittings with the Randles equivalent circuit model (see text).

diffusion constant D is roughly evaluated as $D = 2\pi f_{\mathrm{c}} d^2$.

We quantitatively analyzed CIS using a Randles equivalent circuit model, which consists of the high frequency resistance R_0 of electrolyte, ionic charge-transfer resistance R_{ct}, double layer capacitance C_{dl}, and restricted diffusion impedance ($R_{\mathrm{d}} \times z_{\mathrm{d}}$, where R_{d} and z_{d} are the characteristic resistance and reduced diffusion impedance, respectively) of the flat plate with the thickness d.[52] In order to reproduce the finite slope in the low-frequency region, we used the constant phase element (CPE)-restricted form as z_{d}:[53]

$$z_{\mathrm{d}}(u) = \frac{\alpha u^n + \sqrt{u}\coth\sqrt{u}}{u + \alpha u^{n+1/2}\coth\sqrt{u}}, u = i\frac{\omega d^2}{D}, \tag{3}$$

where ω ($= 2\pi f$), α, and n are the angular velocity, dimensionless quantity, and specific exponent, respectively. Eq. (3) can be derived from Fick's second law,

$$\frac{\partial n}{\partial t} = D\frac{\partial^2 n}{\partial x^2}, \tag{4}$$

and the CPE boundary condition between the active material and the collector electrode. We evaluated seven parameters, *i.e.*, R_0, R_{ct}, C_{dl}, R_{d}, α, n, and D, by least-

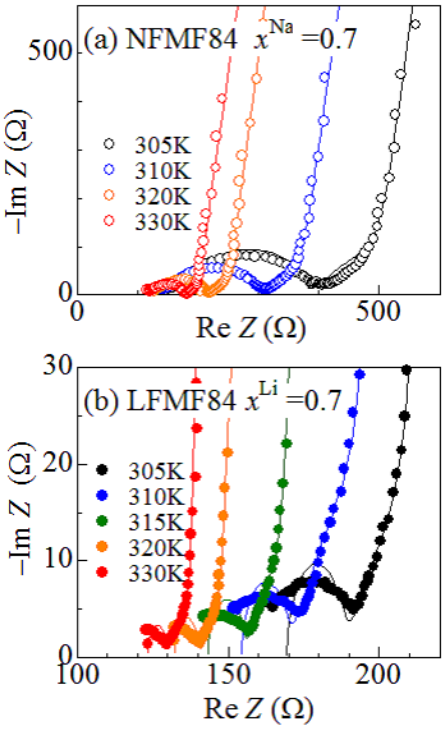

Fig. 5. (Color online) CIS of (a) NMF84 ($x^{Na} = 0.7$) and (b) LMF84 ($x^{Li} = 0.7$) at various temperatures. Solid curves are results of the least-squares fittings with the Randles equivalent circuit model (see text).

squares fittings of the CIS curves [solid curves in Figs. 4(a) and 4(b)].

Figure 5(a) shows the T-dependence of CISs of the NMF84 films at x^{Na} =0.7. The diameter of the semicircle steeply decreases with increasing T, indicating a steep decrease in R_{ct}. A similar behavior is discernible in the LMF84 film at x^{Li} =0.7 [Fig. 5(b)]. The squashed semicircles, however, makes it difficult to precisely evaluate R_{ct}. We investigated the T-dependence of CIS at $x^{Na} = 0.7$, 0.9, and 1.1 using the same NMF84 film ($d = 400$ nm). Similarly, we investigated the T-dependence of CIS at $x^{Li} = 0.7$, 0.9, and 1.1 using the same LMF84 film ($d = 400$ nm).

3.3 Evaluation of E_a^{Na}/E_a^{Li}

In Fig. 6(a), we plotted D^{Na} of the NMF84 films against x^{Na}. Unfortunately, a significant distortion of CIS in the plateau I region ($x^{Na} \leq 0.5$) prevents us from determining D^{Na}. We found that D^{Na} exponentially increases with decreasing T^{-1} as $D^{Na} \propto \exp(-E_a^{Na}/k_B T)$. From the broken straight lines in Fig. 6(a), we evaluated the activation energy E_a^{Na} of D^{Na} by lease-squares fittings. Similarly, we evaluated the activation energy E_a^{Li} of D^{Li} [broken straight lines in Fig. 6(b)]. In Fig. 7, we plotted R_{ct} of the

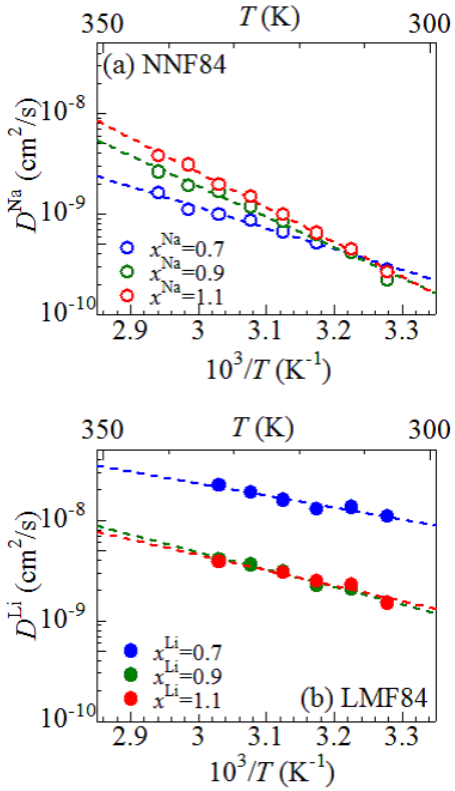

Fig. 6. (Color online) (a) Arrhenius plot of diffusion constant (D^{Na}) of Na^+ in the NMF84 films. Broken straight lines are results of least-squares fittings. (a) Arrhenius plot of diffusion constant (D^{Li}) of Li^+ in the LMF84 films. Broken straight lines are results of least-squares fittings.

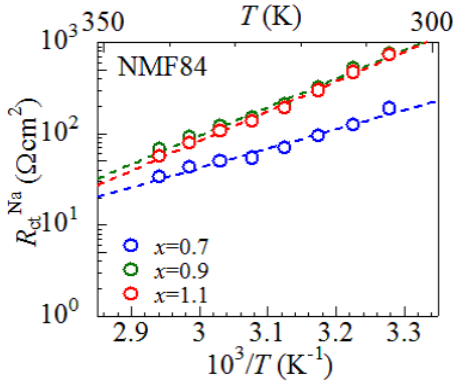

Fig. 7. (Color online) (a) Arrhenius plot of ionic charge-transfer resistance (R_{ct}) of Na^+ in the NMF84 films. Broken straight lines are results of least-squares fittings.

NMF84 films against x^{Na}. We found that R_{ct} exponentially increases with decreasing T^{-1} as $R_{ct} \propto \exp(-E_a^{Na}/k_BT)$. We evaluated the activation energy E_a^{Na} of R_{ct}^{Na} by lease-squares fittings. The squashed semicircles of the LMF84 films make it difficult to precisely evaluate R_{ct}.

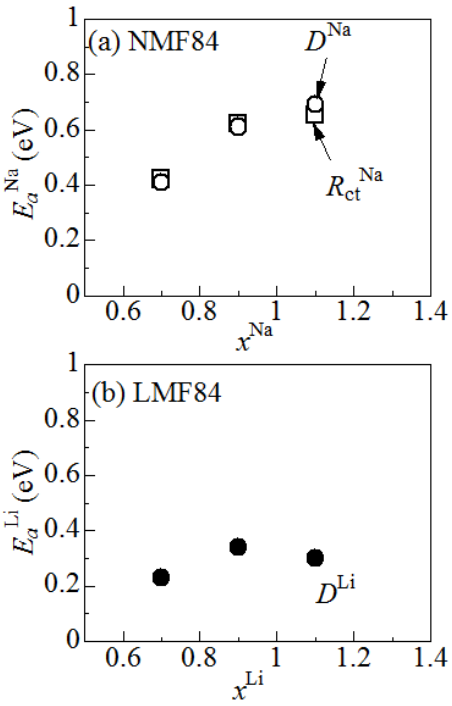

Fig. 8. (a) Activation energies (E_a^{Na}) of D^{Na} (circles) and R_{ct} (squares) in the NMF84 films against x^{Na}. (a) Activation energies (E_a^{Li}) of D^{Li} (circles) in the LMF84 films against x^{Li}.

In Fig. 8(a), we plotted E_a^{Na} (circles) of D^{Na} of the NMF84 films against x^{Na}. We found that E_a^{Na} steeply increases from 0.41 eV at $x^{Na} = 0.7$ to 0.69 eV at 1.1. In Fig. 8(b), we plotted E_a^{Li} of D^{Li} of the LMF84 films against x^{Li}. The increase is suppressed in the LMF84 film: $E_a^{Na} = 0.23$ eV at $x^{Na} = 0.7$ and 0.30 eV at 1.1.

It is interesting that E_a of R_{ct} [squares in Fig. 8(a)] in the NMF84 film is nearly the same as those (circles) of D^{Na}. Generally speaking, the ionic charge-transfer process is divided into (1) the undressing process of the coordinated solvent in electrolyte and (2) the intercalation of undressed ions at the electrolyte/active material interface. The potential barrier of the latter process is essentially the same as that of the ion diffusion. Then, the observation suggests that the ionic charge-transfer process in Mn-HCF is governed by the latter process. Here, we note that the closeness of the two activation energies is also reported in prototypical cathode materials for SIBs, *e.g.*, Na_xCoO_2[54,55] and Na_xMnO_2.[56,57]

Here, let us briefly discuss the physical meaning of the diffusion constant $D(T)$ within the activation energy E_a approximation: $D(T) = D_0\exp(-E_a/k_BT)$. $D(T)$ strongly depends on not only T and but also E_a at $T \ll E_a$ (low-T region) while it is constant ($\approx D_0$) at $T \gg E_a$ (high-T region). Our experimental conditions ($T \sim$

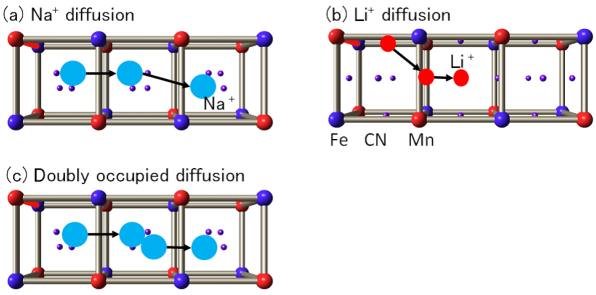

Fig. 9. Schematic illustrations of (a) Na^+ diffusion, (b) Li^+ diffusion, and (c) doubly occupied diffusion. Small spheres represent Na^+/Li^+ sites. Crystal waters are omitted for simplicity.

300 K and $E_a \sim 10^3$ -10^4 K) are in the low-T region. In addition, we observed the x^{Na}-/x^{Li}-dependence of E_a^{Na}/E_a^{Li} [circles in Figs.8 (a) and (b)]. Then, the magnitude of D at a fixed temperature has no well-defined physical meaning because the value is governed by $\exp(-E_a/k_BT)$. In the following section, we will discuss the x^{Li}-/x^{Li}-dependence of E_a^{Na}/E_a^{Li}.

4. Discussion

4.1 Structural effect on E_a^{Na}/E_a^{Li}

Now, let us discuss the origin of the increase in E_a^{Na} with x^{Na} [Fig. 8(a)]. First of all, we should consider the structural effect of the host framework aganist x^{Na}. In the bottom panel of Fig. 1(a), we replotted[21] the lattice constant (a) of the $Na_xMn[Fe(CN)_6]_{0.83}3.5H_2O$ (NMF83) films against x^{Na}. The NMF83 films belong to the face-centered cubic structure in the entire x^{Na}-region ($0.0 \leq x^{Na} \leq 1.32$). In the investigated-$x^{Na}$ region ($0.7 \leq x^{Na} \leq 1.1$), a slightly decreases with x^{Na} from $a = 10.57$ Å at $x^{Na} = 0.7$ to 10.55 Å at 1.1. The compression of the host framework may explain the observed increase in E_a^{Na}, because the compression heightens the single-ion potential barrier between the neighboring Na sites.

This scenario, however, fails to explain the suppressed increase in E_a^{Li} with x^{Li} [Fig. 8(b)]. In the bottom panel of Fig. 1(a), we replotted[30] a of the LMF83 films against x^{Li}. The LMF83 films have the face-centered cubic structure in the entire x^{Li}-region ($0.0 \leq x^{Li} \leq 1.32$). In the investigated x^{Li} region ($0.7 \leq x^{Li} \leq 1.1$), a significantly decreases with x^{Li} from $a = 10.53$ Å at $x^{Li} = 0.7$ to 10.48 Å at 1.1. Such a compression of the host framework would cause steeper increase in E_a^{Li}, which actually is not observed.

4.2 Occupancy effect on E_a^{Na}/E_a^{Li}

Another possible origin for the increase in E_a^{Na} is the occupancy effect of Na^+ sites. Here, let us define the occupancies, g^{Na} ($\equiv x^{Na}/n^{Na}$) and g^{Li} ($\equiv x^{Li}/n^{Li}$), where n^{Na} and n^{Li} are the number of the Na and Li sites per Mn site. Na^+ is located around the tetragonal site close to the central position[47,48] [Fig. 9(a)] Usually, each nanocube accommodates one Na^+ ion and hence $n^{Na} = 2$. As indicated by an arrow, the diffusion path is a straight line between the neighboring Na^+ sites. The potential barrier is located at the face of the nanocube.[58] On the other hand, Matsuda *et al.*[21] performed Rietveld structural analysis of $Li_{0.9}Mn[Fe(CN)_6]_{0.83}3.5H_2O$. They found that the central region of the nanocube is occupied by crystal waters. This strongly suggests that Li^+ is located at the face of the nanotube [Fig. 9(b)] and hence $n^{Na} = 6$. Thus, the Na compound is located in the high-g ($g^{Na} = 0.35$ - 0.55) region, while the Li compound is in the low-g ($g^{Li} = 0.12$ - 0.18) region.

In the high-g region (Na compound), the conventional Na^+ diffusion process is significantly suppressed because most of neighboring Na^+ sites are occupied. In such a case, Na^+ diffusion takes place via the doubly occupied state [Fig. 9(c)]. We will call such a diffusion *doubly occupied diffusion*. Actually, Lee *et al.*[25] reported that the nanocube of $Na_3Mn^{II}[Mn^{I}(CN)_6]$ can statically accommodate two Na^+. The potential barrier for the doubly occupied diffusion [Fig. 9(c)] is considered to be higher than that for the conventional one [Fig. 9(a)]. Thus, the doubly occupied diffusion explains the increase in E_a^{Na} because it becomes dominant with increasing x^{Na}. In the low-g region (Li compound), Li^+ diffusion takes place via the conventional Li^+ diffusion path [Fig. 9(b)] with feeling a single-ion potential barrier. Then, E_a^{Li} is nearly independent of x^{Li} [Fig. 8(b)]

5. Conclusions

We systematically investigated the activation energy E_a^{Li}/E_a^{Na} of D^{Li}/D^{Na} against x^{Na}/x^{Li} in Mn-HCFs. We found that E_a^{Na} increases with x^{Na} from 0.41 eV at $x^{Na} = 0.7$ to 0.69 eV at 1.1. The increase is suppressed in D^{Li}: $E_a^{Na} = 0.23$ eV at $x^{Na} = 0.7$ and 0.30 eV at 1.1. These observations are successfully interpreted in terms of the occupancy effect of guest ions.

Acknowledgments

This work was supported by the Mitsubishi Foundation, Yazaki Memorial Foundation, and Nippon Sheet Glass Foundation. The elementary analyses were performed at the Chemical Analysis Division, Research Facility Center for Science and Engineering, University of Tsukuba. The X-ray absorption experiments were performed at the PF 12C beamline under the approval of the Photon Factory Program Advisory Committee (Proposal No. 2014G501). The XRD measurements were performed at the PF 8B beamline under the approval of the Photon Factory Program Advisory Committee (Proposal No. 2014G507).

References

1) J. M. Tarascon and M. Armand, Nature **414**, 359 (2001).
2) M. Armand and J. M. Tarascon, Nature **451**, 652 (2008).
3) K. Itaya, I. Uchida, and V. D. Neff, Acc. Chem. Res. **19**, 162 (1986).
4) K. Itaya, T. Ataka, and S. Toshima, J. Am. Chem. Soc. **104**, 4767 (1982).
5) B. J. Feldman and O. R. Melroy, J. Electroanal. Chem. **234**, 213 (1987).
6) C. A. Lundgren and R. W. Murray, Inorg. Chem. **27**, 933 (1988).
7) C. Gabrielli, J. J. García-Jareño, M. Keddam, H. Perrot, and F. Vicente, J. Phys. Chem. **106**, 3182 (2002).
8) D. Asakura, C. H. Li, Y. Mizuno, M. Okubo, H. Zhou, and D. R. Talham, J. Am. Chem. Soc. **135**, 2793 (2013).
9) J. Luo, W. Cui, P. He, and Y. Xia, Nat. Chem. **2**, 760 (2010).
10) P. Nie, L. Shen, H. Luo, B. Ding, G. Xu, J. Wang, and X. Zhang, J. Mater. Chem. **2**, 5852 (2014).
11) P. Nie, L. Shen, H. Luo, H. Li, G. Xu, and X. Zhang, Nanoscale **5**, 11087 (2013).
12) N. Imanishi, T. Morikawa, J. Kondo, Y. Takeda, O. Yamamoto, N. Kinugasa, and T. Yamagishi, J. Power Sources **79**, 215 (1999).
13) N. Imanishi, T. Morikawa, J. Kondo, R. Yamane, Y. Takeda, O. Yamamoto, H. Sakaebe, and M. Tabuchi, J. Power Sources **81-82**, 530 (1999).
14) T. Matsuda and Y. Moritomo, Appl. Phys. Express **4**, 047101 (2011).
15) M. Takachi, T. Matsuda and Y. Moritomo, Jpn. J. Appl. Phys. **52**, 044301 (2013).
16) S. Yagi, M. Fukuda, R. Makiura, T. Ichitsubo, and E. Matsubara, J. Mater. Chem. A **2**, 8041 (2013).
17) Y. Mizuno, M. Okubo, E. Hosono, T. Kudo, H. Zhou, K. Ohishi, J. Phys. Chem. C **117**, 10877 (2013).
18) M. Okubo, D. Asakura, Y. Mizuno, J.-D. Kim, T. Mizokawa, T. Kudo, I. Honma, J. Phys. Chem. Lett. **1**, 2063 (2010).
19) Y. Moritomo, M. Takachi, Y. Kurihara, and T. Matsuda, Appl. Phys. Express **5**, 041801 (2012).
20) Y. Lu, L. Wang, J. Cheng, and J. B. Goodenough, Chem. Commun. **48**, 6544 (2012).
21) T, Matsuda, M. Takachi, and Y. Moritomo, Chem. Commun., **49**, 2750 (2013).
22) M. Takachi, T. Matsuda, and Y. Moritomo, Appl. Phys. Express **6**, 025802 (2013).

23) M. Takachi, T. Matsuda, and Y. Moritomo, Jpn. J. Appl. Phys. **53**, 067101 (2014).
24) D. Yang, J. Xu, X.-Z. Liao, Y.-S. He, H. Liu, and Z.-F. Ma, Chem. Commum. **50**, 13377 (2014).
25) H. W. Lee, R. Y. Wang, M. Oasta, S. W. Lee, N. Liu, and Y. Chi, Nat. Commum. **5**, 5280 (2014).
26) L. Wang, J. Song, R. Qiao, L. A, Wray, M. A. Hossain, Y.-D. Chung, W. Yang, Y. Lu, D. Evans, J.-J. Lee, S. Vail, X. Zhao, M. Nishijima, S. Kakimoto, and J. B. Goodenough, J. Am. Chem. Soc. **137**, 2548 (2015).
27) S. Yu, Y. Li, Y. Lu, B. Xu, Q. Wang, M. Yan, and Y. Jing, J. Power Sources **275**, 45 (2015).
28) Y. You, X.-L. Wu, Y.-X. Yin, and Y,-G. Guo, Energy Environ. Sci. **7**, 1643 (2014).
29) L. Wang, Y. Lu, J. Liu, M. Xu, J. Cheng, D. Zhang, and J. B. Goodenough, Angew. Chem. **52**, 1964 (2013).
30) T. Matuda and Y. Moritomo, J. Nanotechnol. **2012**, 568147 (2012).
31) Y. Kurihara, T. Matsuda, and Y. Moritomo:, Jpn. J. Appl. Phys. **52**, 017301 (2013).
32) M. Takachi, Y. Kurihara, and Y. Moritomo, J. Mater. Sci. Eng. **2**, 452 (2012).
33) H. Xia, L. Lu, and G. Ceder, J. Power Sources **159**, 1422 (2006).
34) J. Xie, N. Imanishi, T. Zhang, A. Hirano, Y. Takeda, and O. Yamamoto, Electrochim. Acta **54**, 4631 (2000).
35) S. B. Tang, M. O. Lai, and L. Lu, Mater. Chem. Phys. **111**, 149 (2008).
36) Y. Moritomo, X.-H. Zhu, Y. Kurihara, and T. Matsuda, Jpn. J. Appl. Phys. **51**, 107301 (2012).
37) M. Verdaguer, A. Bleuzen, V. Marvaud, J. Vaissermann, M. Seuleiman, C. Desplanches, A. Scuiller, C. Train, R. Garde, G. Gelly, C. Lomenech, I. Rosenman, P. Veillet, C. Cartier and F. Villain, Coord. Chem. Rev. **190-192**, 1023 (1999).
38) T. Matsuda, J. E. Kim, Y. Moritomo, Phys. Rev. B **79**, 172302 (2009).
39) C. Ling, J. Chen, and F. Mizuno, Phys. Chem. C **117**, 21158 (2013).
40) R. Y. Wang, C. D. Wessells, R. A. Huggins and Y. Cui, Nano Lett. **13**, 5748 (2013).
41) A. Omura and Y. Moritomo, Appl. Phys. Express **5**, 057101 (2012).
42) Y. Moritomo and H. Tanaka: Adv. Condens. Matter. Phys. **2013**, 539620 (2013).
43) T. Shibata and Y. Moritomo, Chem. Commun. **50**, 12941 (2014).
44) T. Shibata, F. Nakada, H. Kamioka, and Y. Moritomo, J. Phys. Soc. Jpn. **77**,

104714 (2008).

45) F. Nakada, H. Kamioka, Y. Moritomo, J. E. Kim, and M. Takata: Phys. Rev. B **77**,(2008) 224436.

46) K. Igarashi, F. Nakada, and Y. Moritomo, Phys. Rev. B **78**, 235106 (2008).

47) Y. Moritomo, T. Matsuda, Y. Kurihara, and J. Kim, J. Phys. Soc. Jpn. **80**, 074608 (2011).

48) Y. Moritomo, T. Matsuda, Y. Kurihara, and J. Kim, J. Phys. Soc. Jpn. **85**, 039001 (2016).

49) M. Takachi and Y. Moritomo, Dalton Trans. **45**, 458 (2016).

50) B. Ravel and M. Newville, J. Synchrotron Radiat. **12**, 537 (2005).

51) Y. Kurihara, H. Funahashi, M. Ishida, N. Hamada, T. Matsuda, K. Igarashi, H. Tanida, T. Uruga, and Y. Moritomo, J. Phys. Soc. Jpn. **79**, 044710 (2010).

52) T. Shibata, Y. Fukuzumi, W. Kobayashi, and Y. Moritomo, Sci.c Rep. **5**, 90006 (2015).

53) J. Bisquert, G, Garcia-Belmonte, F. Fabregat-Santiago, and P. R. Bueno, J. Electroanal. Chem. **475**, 152 (1999)

54) T. Shibata, W. Kobayashi, and Y. Moritomo, Appl. Phys. Express **6**, 097101 (2013).

55) T. Shibata, W. Kobayashi, and Y. Moritomo, Appl. Phys. Express **8**, 029201 (2015).

56) T. Shibata, W. Kobayashi, and Y. Moritomo, Appl. Phys. Express **7**, 067101 (2014).

57) T. Shibata, W. Kobayashi, and Y. Moritomo, Appl. Phys. Express **8**, 029202 (2015).

58) Y. Moritomo and H. Tanaka: Adv. Condens. Matter. Phys. **2013**, 539620 (2013).